Composite Structures 160 (2017) 574–585

Contents lists available at ScienceDirect

Composite Structures

journal homepage: www.elsevier.com/locate/compstruct

A novel auxetic honeycomb with enhanced in-plane stiffness and buckling strength

Ming-Hui Fu, Yu Chen, Ling-Ling Hu *

Department of Applied Mechanics and Engineering, School of Engineering, Sun Yat-sen University, Guangzhou 510275, PR China

ARTICLE INFO

Article history:
Received 8 August 2016
Revised 19 October 2016
Accepted 21 October 2016
Available online 22 October 2016

Keywords:
Auxetic
Honeycomb
In-plane
Elastic properties
Critical buckling strength

ABSTRACT

In the present work, a new design of honeycomb is proposed by embedding the rhombic configuration into the normal re-entrant hexagonal honeycomb (NRHH), in order to enhance the honeycomb's in-plane mechanical properties. Both theoretical analysis and numerical simulations are employed to calculate the in-plane mechanical properties of the new honeycomb under uniaxial compression, including Young's modulus, Poisson's ratio and critical buckling strength. The results show that the new honeycomb can maintain auxetic performance, while both the in-plane Young's modulus and the critical buckling strength are significantly improved compared to the NRHH. Comparisons between the present design and other exiting enhanced periodic topologies are also carried out. With respect to them, the present design features superior performances. For these outstanding properties, this layout may provide a new concept for the optimization and design of auxetic materials.

1. Introduction

As an ultra-light material with physical and structural functions, cellular materials are attractive for use in lightweight structures, energy-absorbing and heat transfer devices [1–6]. For a long time, scientists have focused on revealing the relations between the honeycombs' mechanical properties and their geometric configurations.

In recent years, there is a surge of research into a class of cellular materials with negative Poisson's ratio (NPR) due to their superior physical properties and abnormal characteristics. Re-entrant and roll-up are the two most common mechanisms to achieve negative value of Poisson's ratio. As a typical structure with negative Poisson's ratio, the re-entrant structures, including 2D re-entrant honeycomb and 3D re-entrant lattice, have been extensively studied. Gibson and Ashby [1] developed a seminal model that successfully predicts Young's modulus and Poisson's ratio for conventional hexagonal honeycomb, considering the axial and transverse shear of cell walls as well as bending. A refined cell wall's bending model by adding a beam's stretching and hinging motion was introduced by Masters and Evans [7]. Both the approaches used by Gibson and Ashby [1] and Masters and Evans [7] are able to model the normal re-entrant hexagonal honeycomb (NRHH). Besides, there are other analytical and numerical models to describe the in-plane elastic constants of the NRHH [8,9]. The influences of the cell-wall angle on the indentation resistance of the re-entrant hexagonal honeycombs were studied by Hu and Deng [10] though numerical tests and theoretical analysis. Under large deformation, both the Poisson's ratio [11] and shear modulus [12] of the re-entrant hexagonal honeycombs were investigated systematically. Based on the NRHH, a new 2D centresymmetric honeycomb configuration [13] and a 3D periodic re-entrant lattice structure [14–18] were designed and late studied in deep on their elastic properties.

As well as the elastic properties of cellular materials, collapse is important in applications. According to Gibson and Ashby's work [1], collapse of the cellular materials due to the buckling becomes more likely as relative density is reduced. The asymmetrical buckling mode of three cell edges for conventional hexagonal honeycomb with uniform-thickness cell edges under uniaxial compression was suggested by Gibson and Ashby [1]. Using the similar analytical model, the in-plane elastic buckling strength of regular hexagonal honeycomb with Plateau borders was derived by Chuang and Huang [19]. The theoretical framework for buckling analysis of conventional hexagonal honeycomb used by Gibson and Ashby [1] is able to model the normal re-entrant hexagonal honeycomb (NRHH). Wang and McDowell [2] approximated the buckling strengths of a series of common cellular structures by means of a simplistic approach involving the equivalent beam length for cell walls of different periodic structures (i.e., square cell

* Corresponding author.
E-mail addresses: hulingl@mail.sysu.edu.cn, chuanchi205_sysu@163.com (L.-L. Hu).

http://dx.doi.org/10.1016/j.compstruct.2016.10.090
0263-8223/

honeycomb, triangular cell honeycomb, mixed cell honeycomb, Kagome cell honeycomb, diamond cell honeycomb and rectangular cell honeycomb). In Haghpanah et al.'s work [20], a method based on classical beam-column end-moment behavior expressed in a matrix form was applied to sample honeycombs with square, triangular and hexagonal unit cells to determine their buckling strength under a general macroscopic in-plane stress state. Until now, the research on the in-plane buckling analysis of auxetic structures is rarely reported.

Auxetic materials have been identified in a series of applications in textiles, industry, aerospace, protection, biomedical, sensors and other sectors [21,22]. However, the stiffness of the auxetic materials, which need substantial porosity, is relatively low [22]. Eventually, this causes limitations on the structural applications of the materials with negative Poisson's ratio [23]. Composites incorporating auxetic inclusions were proved to have a great potential in terms of enhanced properties [24]. Also, the gradient honeycombs are promising in improving the in-plane stiffness and some physical properties. With respect to classical re-entrant hexagonal configurations, the thickness gradient re-entrant honeycomb was proved by Lira and Scarpa [25] to have enhanced transverse shear moduli, thermal conductivity and dielectric properties. Continuing further, the graded conventional-auxetic cores and auxetic gradient honeycombs have been proved to have potential in the design of sandwich structures due to their superior performance [26,27]. Recently, in order to improve the in-plane stiffness of the normal re-entrant hexagonal honeycomb (NRHH), two new designs, namely splined-reentrant and stiffened-reentrant honeycombs, were conceived and investigated numerically, experimentally by Zied et al. [28]. For the same purpose, a novel structure was developed by Lu et al. [29] by adding a narrow rib to the unit cell of NRHH. These layouts can be considered as a possible basis to design new concepts of auxetic structures with special functions.

In this paper, a new honeycomb is developed by embedding the rhombic configuration into the normal re-entrant hexagonal honeycomb (NRHH). The effective Young's modulus and Poisson's ratio of the new structure are analytically derived, which is later verified by numerical simulations. Next, parameters studies are conducted by using the numerically validated analytical solutions. Finally, the critical buckling strength of the new proposed honeycomb under uniaxial compression is also studied analytically and numerically.

2. New honeycomb and the representative block

The new honeycomb is developed by the normal re-entrant hexagonal honeycomb (NRHH) with each cell enhanced with four reinforcing walls, as shown in Fig. 1a. The cells within the new honeycomb can also be regarded as a combination of the re-entrant hexagonal configuration and the rhombic configuration. The length of the vertical and the slant walls of the re-entrant cells are h_0 and l_0, respectively, with their thickness being t_0. The thickness and the length of the four reinforcing walls are t_1 and l_1, respectively. The slant walls of the re-entrant hexagonal cells and the reinforcing walls have angles of θ_0 and θ_1 with the horizontal direction, respectively, as marked in Fig. 1. These geometric parameters of the cell walls have relationship with each other, i.e.,

$$l_1 = l_0\sqrt{\frac{h_0^2}{4l_0^2} + \cos^2\theta_0}$$
$$\theta_1 = \arctan\frac{h_0}{2l_0\cos\theta_0}. \tag{1}$$

Under in-plane compression, in view of the periodic symmetry of the honeycomb's cell structure, a representative block is adopted to deduce the mechanical properties of the honeycomb, as marked within the dashed rectangle in Fig. 1a and shown in Fig. 1b in details. The thickness and the length of both FA and CD are $(t_0/2)$ and $(h_0/2)$, respectively.

3. Young's modulus and Poisson's ratio

3.1. Theoretical analysis

When the honeycomb is uniaxially compressed by a stress σ_x along the x-direction, a uniform horizontal displacement u_C will be caused at point B and wall CD, while vertical displacement v_C and v_F will be caused at points C and F, respectively, as shown in Fig. 1b. Due to the periodic symmetry of the cell structure, points A and B have the same vertical displacement, i.e., $v_A = v_B$, and the length of FA and CD after deformation should be equal, i.e.,

$$v_C = v_F - v_A. \tag{2}$$

Since the horizontal planes passing through points A and D are the plane of symmetry, the transverse shear stress at points A and D are zero that there is no transverse shear force on the vertical walls FA and CD. For the reinforcing walls, the axial deformation is the primary mechanism as every two neighboring reinforcing

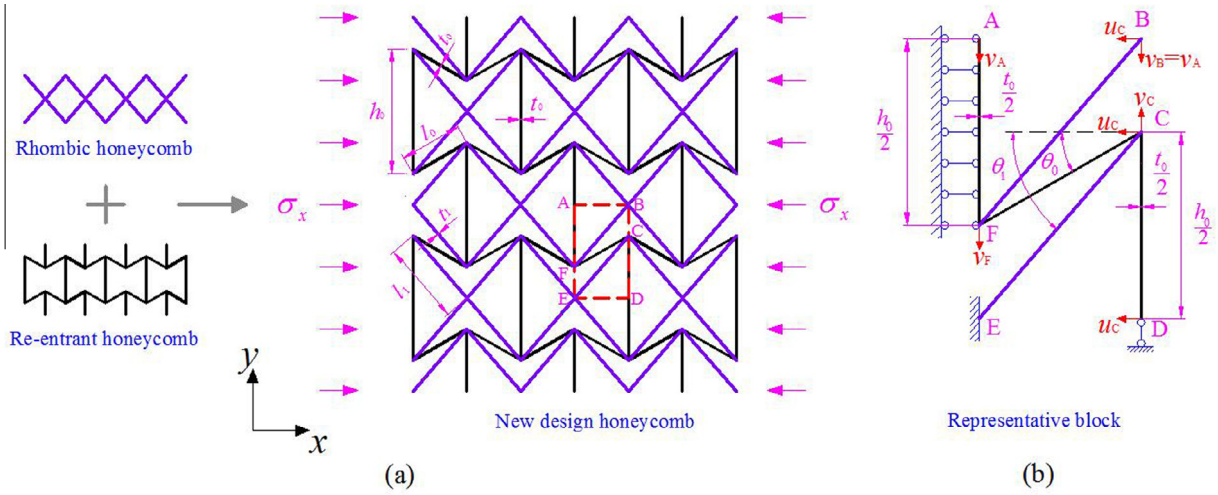

Fig. 1. New honeycomb (a) cells' geometry and (b) representative block.

walls form a triangle with the adjacent vertical wall. Thus, the transverse shear force and the end-point bending moment on the reinforcing walls can be neglected.

The axial force of both the two vertical walls and the two reinforcing walls in Fig. 1b can be derived by the end-point displacement of the respective wall. The axial force on the walls FA and CD is

$$F_{FA}^N = F_{CD}^N = \frac{E_0 b t_0}{h_0} v_C, \tag{3}$$

with E_0 being Young's modulus of the walls in normal re-entrant cells, and b being the width of the honeycomb in the out-of-plane direction. The axial force on the reinforcing walls FB and EC are

$$F_{FB}^N = F_{EC}^N = \frac{E_1 b t_1}{l_1}(u_C \cos\theta_1 - v_C \sin\theta_1), \tag{4}$$

with E_1 being Young's modulus of the reinforcing walls.

For the slant wall FC, both the bending deformation and the transverse shear deformation should be considered besides the axial deformation, as shown in Fig. 2. The axial force on wall FC is

$$F_{FC}^N = \frac{E_0 b t_0}{l_0}[u_C \cos\theta_0 - (v_C + v_F)\sin\theta_0]. \tag{5}$$

The transverse shear force on FC depends on the relative displacement between C and C′, δ, and δ is:

$$\delta = u_C \sin\theta_0 + (v_C + v_F)\cos\theta_0. \tag{6}$$

A 3D periodic re-entrant lattice structure designed by fourfold rotations of the bow-tie functional element was analytically investigated by Yang et al. [16]. Both the bending-induced deflection and the shear-induced deflection of the slant strut were considered. Following similar approach used by Yang et al. [16], the deflection angles θ_F and θ_C in Fig. 2 can be expressed as

$$\theta_F = \theta_C = \frac{M l_0}{6E_0 I_0} + \frac{F_{FC}^S}{\kappa G_0 A_0}, \tag{7}$$

with $M = M_{FC} = M_{CF} = F_{FC}^S l_0/2$, where $G_0 = E_0/(2+2\mu_0)$ is the shear modulus of the basic re-entrant cell wall with μ_0 being its Poisson's ratio, $A_0 = bt_0$ is the cross section area of wall FC, and $I_0 = bt_0^3/12$ is the second moment of inertia of the cross section. For rectangular cross section, $\kappa = 5/6$.

Under small deformation, wall FC deflects by:

$$\delta \approx l_0\theta_F = \frac{l_0^3}{12E_0 I_0}F_{FC}^S + \frac{l_0}{\kappa G_0 A_0}F_{FC}^S. \tag{8}$$

Thus, the transverse shear force on FC can be obtained by substituting Eq. (6) into Eq. (8):

$$F_{FC}^S = \frac{E_0 b (t_0/l_0)^3 [u_C \sin\theta_0 + (v_C + v_F)\cos\theta_0]}{1 + 2.4(1+\mu_0)(t_0/l_0)^2}. \tag{9}$$

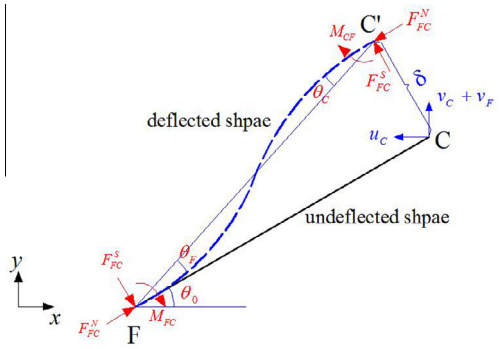

Fig. 2. Deformation of wall FC.

In the following, the end-point displacements v_A, v_B, v_C and v_F will be expressed as function of displacement u_C by using the force balance conditions. Since the honeycomb is free along the y-direction, the total y-directional force on the top boundary of the representative block must be zero, i.e.,

$$F_{FB}^N \sin\theta_1 - F_{FA}^N = 0. \tag{10}$$

By substituting Eqs. (3) and (4) into Eq. (10), the vertical displacement v_C is

$$v_C = \frac{\sin\theta_1 \cos\theta_1 E_1 t_1/l_1}{E_0 t_0/h_0 + \sin^2\theta_1 E_1 t_1/l_1} u_C. \tag{11}$$

Based on the force balance on point F along the y-direction, it is obtained:

$$F_{FC}^N \sin\theta_0 - F_{FC}^S \cos\theta_0 + F_{FB}^N \sin\theta_1 - F_{FA}^N = 0. \tag{12}$$

By substituting Eq. (10) into Eq. (12), we have:

$$F_{FC}^N \sin\theta_0 - F_{FC}^S \cos\theta_0 = 0. \tag{13}$$

Then, v_F can be obtained by substituting Eqs. (5) and (9) into Eq. (13):

$$\begin{aligned} v_F = {} & \frac{[1 + (1.4 + 2.4\mu_0)(t_0/l_0)^2]\sin\theta_0\cos\theta_0}{(t_0/l_0)^2\cos^2\theta_0 + [1 + 2.4(1+\mu_0)(t_0/l_0)^2]\sin^2\theta_0} u_C \\ & - \frac{\sin\theta_1\cos\theta_1 E_1 t_1/l_1}{E_0 t_0/h_0 + \sin^2\theta_1 E_1 t_1/l_1} u_C. \end{aligned} \tag{14}$$

According to the force balance along the x-direction on the right boundary of the representative block, we have

$$\begin{aligned} & F_{FC}^N \cos\theta_0 + F_{FC}^S \sin\theta_0 + F_{EC}^N \cos\theta_1 + F_{FB}^N \cos\theta_1 \\ & = \sigma_x (h_0 - l_0 \sin\theta_0) b. \end{aligned} \tag{15}$$

Thus,

$$\sigma_x = \frac{K_1 + K_2}{h_0 - l_0 \sin\theta_0} u_C, \tag{16}$$

with

$$\begin{aligned} K_1 = {} & \frac{\cos^2\theta_0 E_0 t_0}{l_0} + \frac{E_0 (t_0/l_0)^3 \sin^2\theta_0}{1 + 2.4(1+\mu_0)(t_0/l_0)^2} \\ & + \frac{2\cos^2\theta_1 E_1 t_1}{l_1} - \frac{2(\sin\theta_1\cos\theta_1 E_1 t_1/l_1)^2}{E_0 t_0/h_0 + \sin^2\theta_1 E_1 t_1/l_1}, \end{aligned}$$

$$\begin{aligned} K_2 = {} & \frac{\sin^2\theta_0 \cos^2\theta_0 E_0 t_0/l_0}{1 + 2.4(1+\mu_0)(t_0/l_0)^2} \\ & \times \frac{-[1 + (1.4 + 2.4\mu_0)(t_0/l_0)^2]^2}{(t_0/l_0)^2\cos^2\theta_0 + [1 + 2.4(1+\mu_0)(t_0/l_0)^2]\sin^2\theta_0}. \end{aligned}$$

Obviously, K_1 and K_2 only depend on the cell walls' modulus and the geometric parameters of the cell, including θ_0 , θ_1, t_0, l_0, h_0, t_1 and l_1.

The effective strain along the x-direction, ε_x, is giving by:

$$\varepsilon_x = \frac{u_C}{l_0 \cos\theta_0}. \tag{17}$$

The effective strain along the y-direction, ε_y, is:

$$\begin{aligned} \varepsilon_y = \frac{v_A}{h_0 - l_0\sin\theta_0} = {} & -\frac{2\sin\theta_1\cos\theta_1 E_1 t_1/l_1}{(E_0 t_0/h_0 + \sin^2\theta_1 E_1 t_1/l_1) l_0 (h_0/l_0 - \sin\theta_0)} u_C \\ & + \frac{[1 + (1.4 + 2.4\mu_0)(t_0/l_0)^2]\sin\theta_0\cos\theta_0}{\left\{(t_0/l_0)^2\cos^2\theta_0 + [1 + 2.4(1+\mu_0)(t_0/l_0)^2]\sin^2\theta_0\right\} l_0 (h_0/l_0 - \sin\theta_0)} u_C. \end{aligned} \tag{18}$$

Thus, the effective Young's modulus, E_x and effective Poisson's ratio, μ_{xy} are obtained as:

$$E_x = \frac{(K_1 + K_2)\cos\theta_0}{(h_0/l_0 - \sin\theta_0)}, \tag{19}$$

and

$$\mu_{xy} = -\frac{\varepsilon_y}{\varepsilon_x} = \frac{2\sin\theta_1\cos\theta_1\cos\theta_0 E_1 t_1/l_1}{(E_0 t_0/h_0 + \sin^2\theta_1 E_1 t_1/l_1)(h_0/l_0 - \sin\theta_0)} - \frac{[1 + (1.4 + 2.4\mu_0)(t_0/l_0)^2]\sin\theta_0\cos^2\theta_0}{\left\{(t_0/l_0)^2\cos^2\theta_0 + [1 + 2.4(1+\mu_0)(t_0/l_0)^2]\sin^2\theta_0\right\}(h_0/l_0 - \sin\theta_0)}, \tag{20}$$

respectively.

By using a similar method adopted above, when compressed along the y-direction, the honeycomb's effective Young's modulus, E_y, and Poisson's ratio, μ_{yx}, can also be obtained correspondingly. The derivation is shown in Appendix A in details.

3.2. Finite element analysis

In order to verify the analytical results obtained above, numerical simulations are conducted by using ANSYS. The numerical models of the new honeycomb contain 8×8 unit cells with $\theta_0 = 30°$, $h_0/l_0 = 2$ and $t_0 = t_1 = 1$ mm, as shown in Fig. 3. The out-of-plane thickness of the honeycomb block, b, is 1 mm. Nine levels of slant wall length, l_0, are adopted: 10 mm, 15 mm, 20 mm, 25 mm, 30 mm, 40 mm, 50 mm, 80 mm and 100 mm.

The boundary conditions of the honeycomb block are shown in Fig. 3. When the honeycomb block is compressed along the x-direction, both the horizontal displacement of the nodes at the left boundary and the vertical displacement of the nodes at the bottom boundary of the block are constrained. A uniform displacement Δu_x is imposed on the nodes at the right boundary of the block, while the nodes at the top boundary are coupled to move freely along the y-direction. Similarly, when the honeycomb block is compressed along the y-direction, both the horizontal displacements of the nodes at the left and the vertical displacement of the nodes at the bottom of the honeycomb block are constrained. A uniform displacement Δu_y is imposed on the nodes at the top of the block, while the nodes on the right boundary are coupled together to move freely along the x-direction. The out-of-plane displacements are constrained for all nodes.

Aluminum alloy is used for the cell wall material with $E_0 = E_1 = 70$ GPa and $\mu_0 = \mu_1 = 0.33$. The cell walls are meshed by the beam element of BEAM 188 with an element size of 0.5 mm. A mesh sensitivity analysis is carried out to ensure that the numerical solutions are mesh-independent.

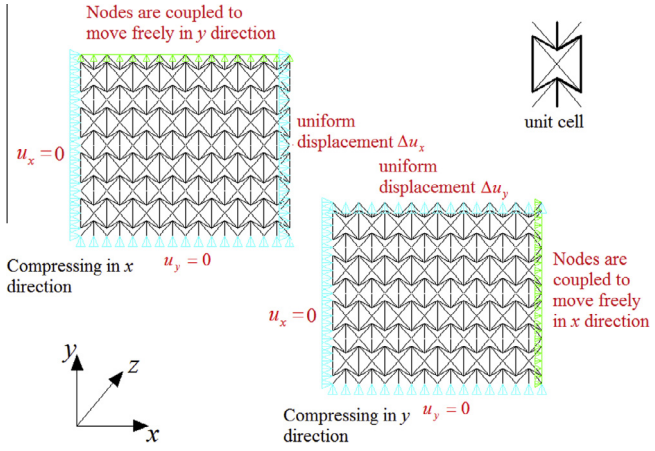

Fig. 3. Boundary conditions used in the numerical models.

For normal re-entrant hexagonal honeycomb (NRHH), the in-plane Young's modulus and Poisson's ratio were derived by Gibson and Ashby [1] by considering all the three mechanisms of bending, shearing and stretching,

$$\begin{aligned}
E_x^* &= \frac{E_0 t_0^3}{l_0^3}\frac{\cos\theta_0}{(h_0/l_0 - \sin\theta_0)\sin^2\theta_0}\frac{1}{1 + (2.4 + 1.5\mu_0 + cot^2\theta_0)(t_0/l_0)^2} \\
E_y^* &= \frac{E_0 t_0^3}{l_0^3}\frac{(h_0/l_0 - \sin\theta_0)}{\cos^3\theta_0}\frac{1}{1 + [2.4 + 1.5\mu_0 + \tan^2\theta_0 + 2(h_0/l_0)/\cos^2\theta_0](t_0/l_0)^2} \\
\mu_{xy}^* &= \frac{-\cos^2\theta_0}{(h_0/l_0 - \sin\theta_0)\sin\theta_0}\frac{1 + (1.4 + 1.5\mu_0)(t_0/l_0)^2}{1 + (2.4 + 1.5\mu_0 + \cot^2\theta_0)(t_0/l_0)^2} \\
\mu_{yx}^* &= \frac{-\sin\theta_0(h_0/l_0 - \sin\theta_0)}{\cos^2\theta_0}\frac{1 + (1.4 + 1.5\mu_0)(t_0/l_0)^2}{1 + [2.4 + 1.5\mu_0 + \tan^2\theta_0 + 2(h_0/l_0)/\cos^2\theta_0](t_0/l_0)^2},
\end{aligned} \tag{21}$$

where E_x^* and μ_{xy}^* are Young's modulus and Poisson's ratio of the NRHH, respectively, when it is uniaxially compressed along the x-direction, and E_y^*, μ_{yx}^* are those when it is under uniaxial compression along the y-direction.

Here, in-plane stiffness ratios of β_x and β_y are introduced to evaluate the enhancement of the in-plane stiffness of the new honeycomb with respect to that of NRHH. β_x and β_y are giving by:

$$\begin{aligned}
\beta_x &= E_x/E_x^* \\
\beta_y &= E_y/E_y^*.
\end{aligned} \tag{22}$$

Fig. 4 compares the numerical and the analytical results of the in-plane stiffness ratio β and Poisson's ratio μ of the new honeycomb with various t_0/l_0, indicating that the analytical results are in well agreement with the numerical ones. According to the results obtained by Gibson and Ashby [1], in the case of NRHH, when $h_0/l_0 = 2, \theta_0 = 30°$, $E_x^* \approx E_y^*$ and $\mu_{xy}^* \approx \mu_{yx}^*$, which resulted in transversely isotropic characteristic. Coincidentally, the new honeycomb also exhibits transversely isotropic characteristic with $\beta_x \approx \beta_y (E_x \approx E_y)$ and $\mu_{xy} \approx \mu_{yx}$ when $h_0/l_0 = 2, \theta_0 = 30°$.

As shown in Fig. 4a, β_x and β_y are both higher than 1, and increase significantly with the decrease of the cell-wall thickness ratio t_0/l_0 (when $t_0/l_0 = 0.01$, $\beta_x \approx \beta_y \approx 871$), which indicates that the in-plane stiffness of the new honeycomb is indeed improved significantly compared to the NRHH.

It is shown in Fig. 4b that both the analytical and the numerical results demonstrate auxetic performance of the new proposed design, although the magnitude of Poisson's ratio of the new proposed honeycomb is reduced with respect to the NRHH. It can be explained by the cells' configuration of the new honeycomb, i.e., the combination of normal re-entrant hexagonal configuration and rhombic configuration, as shown in Fig. 1a. A honeycomb with rhombic cells exhibits positive Poisson's ratio under uniaxial in-plane compression, which weakens the auxetic performance of the re-entrant hexagonal cell. Besides, it is shown in Fig. 4b that both μ_{xy} and μ_{yx} decrease with the increase of the ratio t_0/l_0.

3.3. Parametric studies and discussions

In the following, the effects of the cell's geometric parameters on the in-plane elastic properties are explored based on the analytical solutions obtained in Section 3.1.

Fig. 5 displays the effect of the re-entrant angle, θ_0, on the in-plane properties of the new honeycomb with three different levels of t_1/t_0. It is shown in Fig. 5a that the in-plane stiffness ratios, β_x and β_y , increase with θ_0 until to a peak and then decrease. The peak appears with $\theta_0 \approx 50°$ for all the cases, revealing that the new honeycomb can achieve the best effect of stiffness enhancement near $\theta_0 = 50°$. In addition, it is shown in Fig. 5a that both β_x and β_y

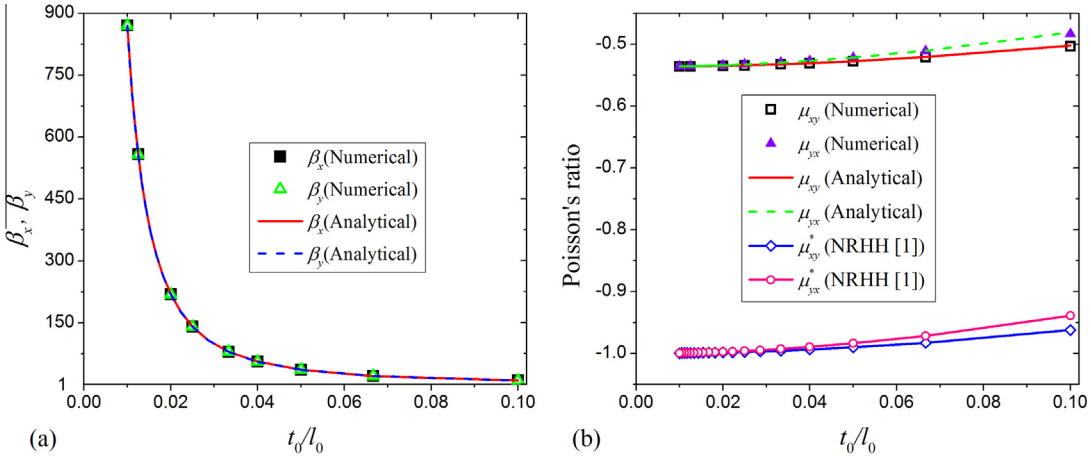

Fig. 4. Variation of in-plane elastic properties of the new honeycomb with t_0/l_0 ($\theta_0 = 30^\circ, h_0/l_0 = 2, t_0 = t_1 = 1$) (a) in-plane stiffness ratio and (b) Poisson's ratio.

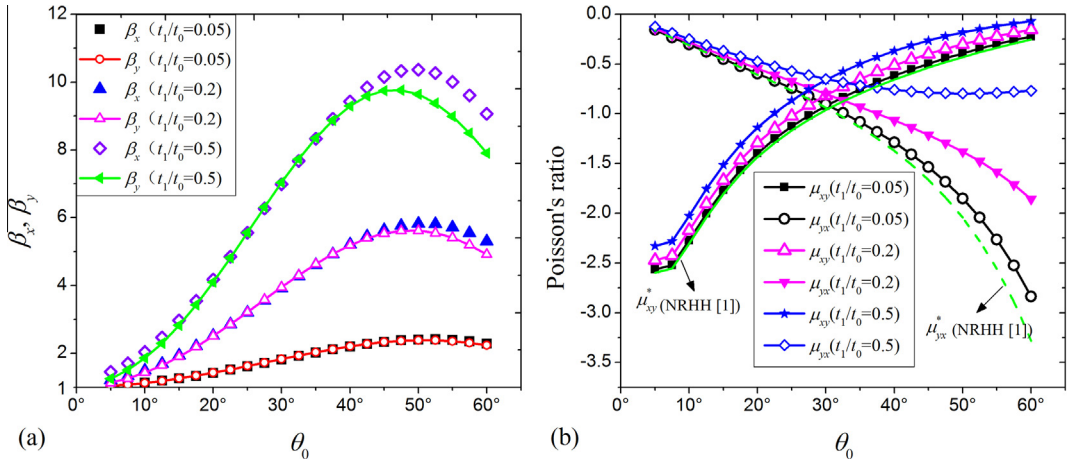

Fig. 5. Variation of the new honeycomb's in-plane elastic properties with re-entrant angle θ_0 ($h_0/l_0 = 2, t_0 = 1, l_0 = 10$) (a) in-plane stiffness ratio and (b) Poisson's ratio.

increase with t_1/t_0, indicating that the thicker of the reinforcing walls are, the more obvious enhanced effect on the new honeycomb's stiffness in comparison to the NRHH.

However, the thicker of the reinforcing walls are, the weaker of the auxetic performance of the new honeycomb, as shown in Fig. 5b. The Poisson's ratios of the new honeycombs with $t_1/t_0 = 0.05$ are very close to that of the NRHH. Besides, it is shown in Fig. 5b that with increase of re-entrant angle θ_0, μ_{xy} decrease while μ_{yx} increase. Noticing that, for different of t_1/t_0, $\mu_{xy} \approx \mu_{yx}$ at $\theta_0 = 30^\circ$, indicating the transversely isotropic characteristic of the new honeycomb, as discussed in the last section (Fig. 4).

The effect of the cell-wall length ratio, h_0/l_0, on the in-plane stiffness ratio and Poisson's ratio is displayed in Fig. 6. It is shown that both β_x and β_y decrease with the increase of h_0/l_0, see Fig. 6a. It

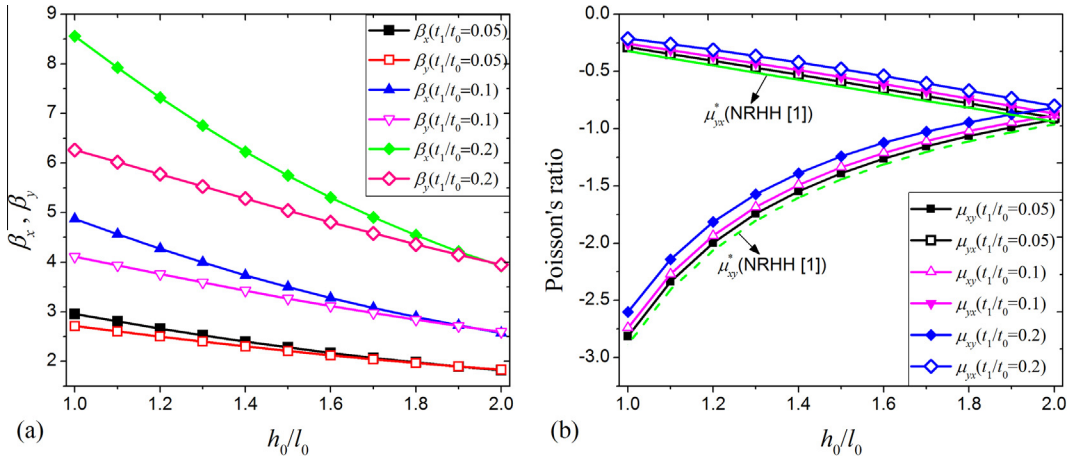

Fig. 6. Variation of the in-plane elastic properties of the new honeycomb with h_0/l_0 ($\theta_0 = 30^\circ, t_0 = 1, l_0 = 10$) (a) in-plane stiffness ratio and (b) Poisson's ratio.

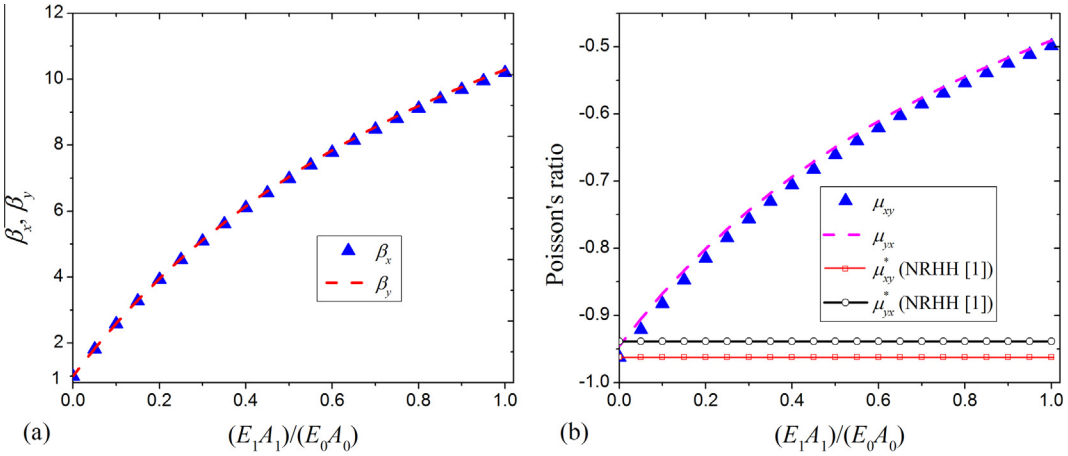

Fig. 7. Variation of the in-plane elastic properties of the new structure with $(E_1A_1)/(E_0A_0)$ $(\theta_0 = 30^\circ, h_0/l_0 = 2, t_0 = 1, l_0 = 10)$ (a) in-plane stiffness ratio and (b) Poisson's ratio.

is shown in Fig. 6b that with the increase of h_0/l_0, the new honeycomb's Poisson's ratio μ_{xy} decreases while μ_{yx} increases, which are similar to that of the NRHH.

By remaining the $h_0/l_0 = 2$, $\theta_0 = 30^\circ$, $t_0 = 1$ and $l_0 = 10$, the effect of the normalized axial rigidity of the reinforcing walls, $(E_1A_1)/(E_0A_0)$, on the in-plane elastic properties is displayed in Fig. 7. It is noted that, when $(E_1A_1)/(E_0A_0)$ is equal to zero, $\beta_x = \beta_y = 1$, $\mu_{xy} = \mu^*_{xy}$, $\mu_{yx} = \mu^*_{yx}$, indicating that the new honeycomb will reduce to the NRHH with $(E_1A_1)/(E_0A_0)$ being zero. It also can be seen that, with the increase of $(E_1A_1)/(E_0A_0)$, the in-plane stiffness ratios, β_x and β_y, increase, while the Poisson's ratio μ_{xy} and μ_{yx} decrease. As a result, the in-plane stiffness of the new honeycomb is improved significantly compared to the NRHH on account of the reinforcing walls. However, at the same time, the reinforcing walls will weaken the auxetic performance of the honeycomb. That is, the larger normalized axial rigidity, $(E_1A_1)/(E_0A_0)$, of the reinforcing walls is, the more obvious the in-plane stiffness enhancement, while the weaker the negative Poisson's ratio effect. Therefore, the reinforcing walls should be designed with appropriate normalized axial rigidity to balance the enhanced stiffness and the superior auxetic performance.

Typically, the aim of cellular structural designs is to maximize the stiffness and/or strength to relative density. However, the trade-off between in-plane stiffness and auxetic performance should be taken into consideration seriously on the aspects of structures with negative Poisson's ratio. Fig. 8 compares the normalized Young's modulus (normalized by cell wall material's Young's modulus) and the Poisson's ratio of the present design with that of other designs in literatures.

The relative density of the normal re-entrant hexagonal honeycomb (NRHH) is calculated as [1]

$$\frac{\rho^*}{\rho_0} = \frac{(h_0/l_0 + 2)(t_0/l_0)}{2\cos\theta_0(h_0/l_0 - \sin\theta_0)}, \tag{23}$$

and the relative density of the new honeycomb designed in this paper is

$$\frac{\rho^*}{\rho_0} = \frac{(h_0/l_0 + 2)(t_0/l_0) + [(h_0/l_0)^2 + 4\cos^2\theta_0](t_1/l_1)}{2\cos\theta_0(h_0/l_0 - \sin\theta_0)}, \tag{24}$$

where ρ^* and ρ_0 are the density of the honeycomb and the cell-wall material, respectively.

It is remarkable that, in both the x- and the y- direction, the in-plane stiffness of the structure developed by Lu et al. [29] is significantly higher than that of others under the same relative density, while the splined re-entrant [28] structure features the lowest stiffness, as shown in Fig. 8a and b. With respect to the NRHH, both the present design and the stiffened re-entrant structure perform higher in-plane stiffness. When compressed along the y direction, the present design exhibits higher Young's modulus than the stiffened re-entrant structure [28] for $\rho^*/\rho_0 < 0.1425$ and lower for $\rho^*/\rho_0 > 0.1425$ (see Fig. 8b), while the Young's modulus in the x-direction of it is always higher than that of the stiffened re-entrant structure [28], as shown in Fig. 8a.

Both the present study and Lu et al.' work [29] show that, with increase of the thickness of the reinforcing walls, the honeycomb's in-plane stiffness increases, while the negative-Poisson's-ratio effect decreases. By changing the thickness of the reinforcing walls only, Fig. 8c displays the effect of the Poisson's ratio on the normalized Young's modulus with $\theta_0 = 30^\circ$ and $h_0/l_0 = 2, t_0/l_0 = 0.05$. It is shown that, under the same value of Poisson's ratio, the normalized Young's modulus in the x direction of the present design, E_x/E_0, is higher than that of the Lu et al.' design [29], while the normalized Young's modulus in the y direction of it,E_y/E_0, is lower than that of the Lu et al.' design [29]. Obviously, the present design performs isotropic characteristic (E_x/E_0 is very close to E_y/E_0), whereas the structure proposed by Lu et al. [29] displays great different characteristics between the x- and the y-direction.

According to the results derived by Gibson and Ashby [1], the dependence of normalized Young's modulus on relative density of the NRHH can be expressed in the following form:

$$(E^*_x/E_0) \propto (\rho^*/\rho_0)^3, \tag{25}$$

which is consistent to the curves shown in Fig. 8a and b. However, for both the present design and the Lu et al.' design [29], approximately linear relationship is exhibited between $\bar{E}/E_0$ and ρ^*/ρ_0. Therefore, the normalized Young's modulus of both the present design and Lu et al.' design [29] can be expressed as

$$(\bar{E}/E_0) \propto (\rho^*/\rho_0). \tag{26}$$

For cellular materials, the general dependences of the stiffness such as relative Young's modulus $\hat{E}/E_0$ on relative density $\hat{\rho}/\rho_0$ were summarized by Grenestedt [30]. The result is given as

$$(\hat{E}/E_0) \propto (\hat{\rho}/\rho_0)^m, \tag{27}$$

in which $m = 3$, e.g., Eq. (25), for bending controlled micro structures and $m = 1$, e.g., Eq. (26), if the axial deformation is dominated in the micro structures. Unlike the bending controlled micro struc-

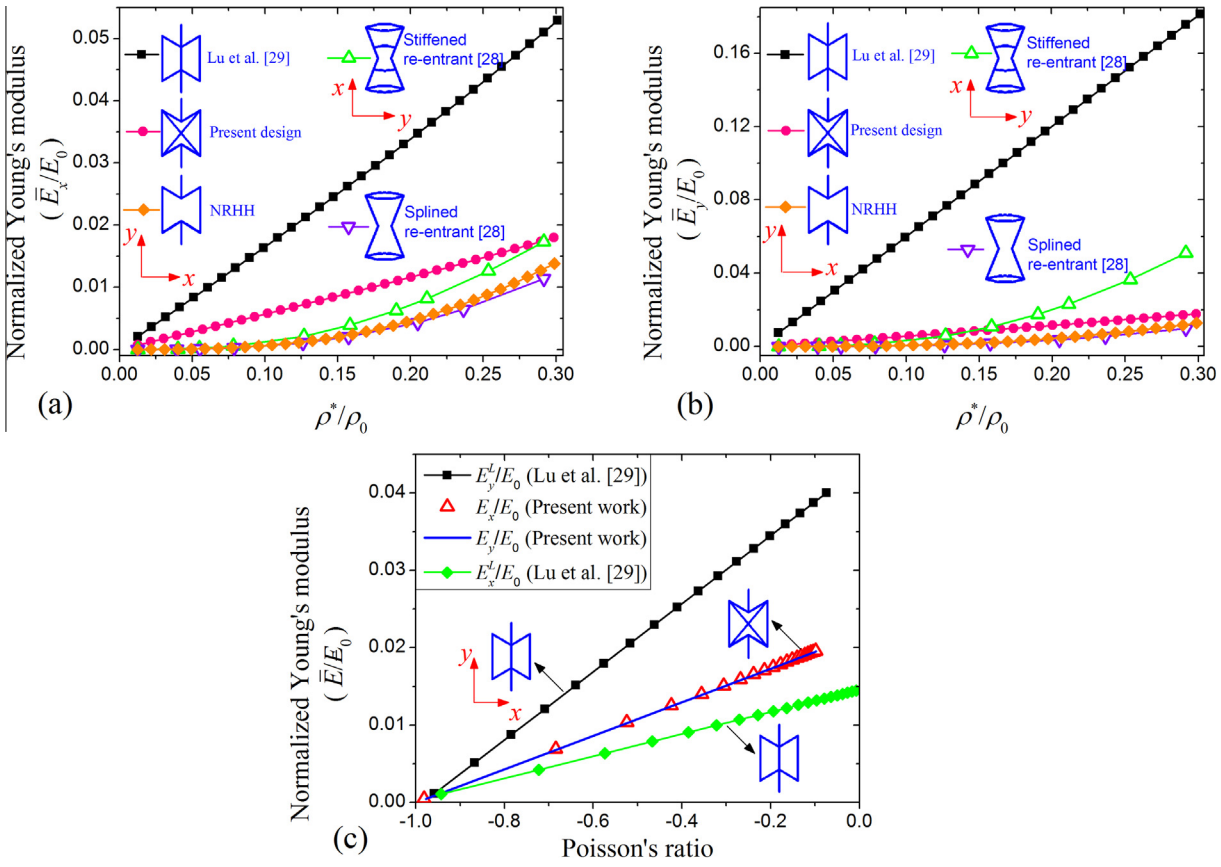

Fig. 8. Comparisons of Young's modulus of various periodic topologies ($\theta_0 = 30°, E_1 = E_0, \mu_1 = \mu_0, h_0/l_0 = 2$) (a) $\bar{E}_x/E_0$ vs. ρ^*/ρ_0 (b) $\bar{E}_y/E_0$ vs. ρ^*/ρ_0 and (c) normalized Young's modulus vs. Poisson's ratio.

ture in NRHH, axial deformation is dominated in both the present design and Lu et al.'s design [29].

4. Buckling strength

As discussed in Section 3.3, in order to maintain the superior auxetic performance, the reinforcing walls should not be designed with very high axial rigidity. Thus, the reinforcing walls with $E_1 = E_0, \mu_1 = \mu_0$ and $t_1 = 0.5t_0$ are adopted to investigate the critical buckling strength of the new honeycomb. When the new honeycomb is subjected to compressive load with sufficient magnitude along the vertical walls, buckling is intend to occur both in the vertical walls and the reinforcing walls. It will be failure when the buckling occurs both in the reinforcing and the vertical walls.

To understand the bulking models of the cell walls, numerical simulations on both the new honeycomb and the normal re-entrant hexagonal honeycomb (NRHH) are carried out by using ANSYS. The numerical models of the new honeycomb containing 8×8 unit cells with $h_0/l_0 = 2$, $l_0 = 10$ mm, $t_0 = 1$ mm and $t_1 = 0.5$ mm are shown in Fig. 9. The out-of-plane thickness of the blocks $b = 1$ mm, and three levels of re-entrant angle θ_0 are adopted: 10°, 30° and 45°. The boundary conditions of the blocks are shown in Fig. 9 in details. The vertical displacement of the nodes at the bottom of the honeycomb block and the horizontal displacement of the middle nodes at the bottom are all constrained. A uniform vertical downward displacement is imposed on the top, and the out-of-plane displacements are constrained for all nodes. The cell-wall material of both kinds of honeycombs is taken as an aluminum alloy with $E_0 = E_1 = 70$ GPa and $\mu_0 = \mu_1 = 0.33$. Beam element of BEAM 188 with an element size

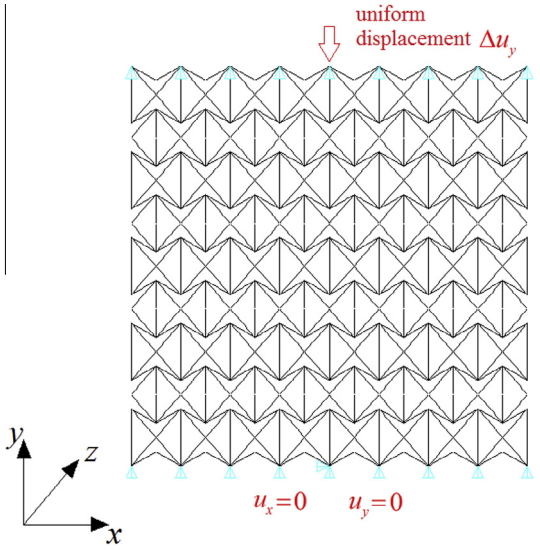

Fig. 9. Numerical model used to evaluate the critical buckling strength.

of 2 mm is used to mesh the cell walls. The verification of mesh density is conducted during this work. The numerical model for NRHH is similar to that of the new honeycomb except for the lack of the enhancing walls.

The buckling models of both the NRHH and the new honeycomb are displayed in Fig.10a and b, respectively. It is obvious that the buckling models of the vertical walls of the two honeycombs are different. The vertical walls in the NRHH perform in "S" shape with

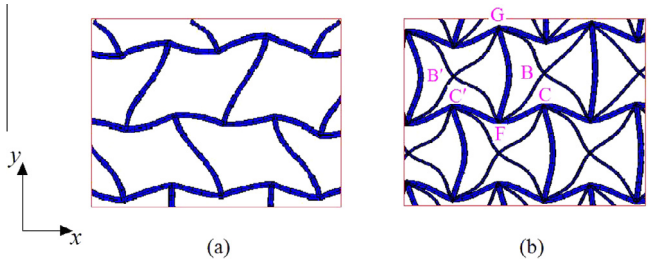

Fig. 10. Buckling models of cell walls in numerical simulations (a) normal re-entrant hexagonal honeycomb (NRHH) (b) new honeycomb.

an obvious relative displacement along the horizontal direction between the two end points of the vertical walls, as shown in Fig. 10a. However, on account of the restraint of the reinforcing walls in the new honeycomb, there is almost no relative horizontal displacement between the two end points of the vertical walls, so the vertical walls in the new honeycomb perform in "bow" shape, as shown in Fig. 10b. Similar to the vertical walls, the "bow" shape also appears in the reinforcing walls of the deformed new honeycomb.

Based on the buckling model observed in the numerical simulations (Fig. 10b), the deformed cell walls are focused and shown in Fig. 11 for theoretical analysis. All the walls in Fig. 11a rotate an equal angle ϕ at F. The vertical wall FG is assumed to be an Euler compressive bar with elastic supports at two ends (see Fig. 11b). And it suffers from a moment of M at each end. Then the rotational stiffness S at joint F is calculated as

$$S = \frac{M}{\phi} = \frac{M_1 + M_2 + M_3 + M_5}{\phi}. \tag{28}$$

In the case with small value of t_1/t_0 concerned here, the stiffness of walls FB and FB', is much less than that of walls FC and FC', i.e., $\frac{M_3+M_5}{\phi} << \frac{M_1+M_2}{\phi}$, thus, Eq. (28) can be approximate to

$$S \approx \frac{M_1 + M_2}{\phi}. \tag{29}$$

By relating the end slope of cell wall FC (FC') to moments acting on it gives,

$$M_1 + M_2 = \frac{4E_0 I_0 \phi}{l_0}. \tag{30}$$

Substituting Eq. (30) into Eq. (29), we obtain:

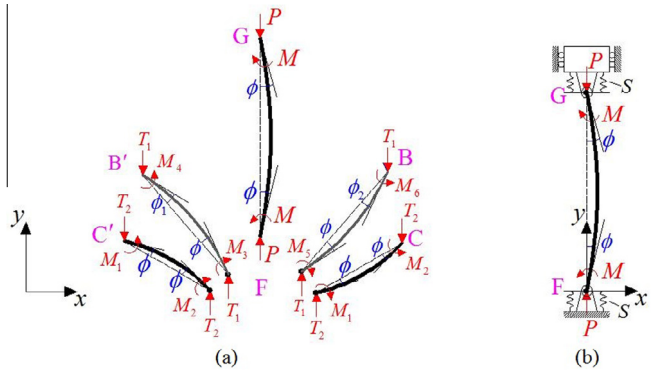

Fig. 11. Analytical model for the bucking analysis of the new honeycomb (a) representative unit and the associated forces, moments, displacement and rotations (b) vertical wall FG can be treated as an Euler compressive bar with elastic supports at two ends.

$$S \approx \frac{4E_0 I_0}{l_0}. \tag{31}$$

Following the method used by Timoshenko and Gere [31], the deflection equation of the vertical wall FG after deformation can be found to be

$$x = A\sin(\lambda y) + B\cos(\lambda y) + \frac{M}{P}, \tag{32}$$

where A and B being arbitrary constants which are unique for a given set of boundary conditions and $\lambda = \sqrt{\frac{P}{E_0 I_0'}}$ ($I_0' = I_0 = bt_0^3/12$ is the second moment of inertia of the cross section of the vertical wall FG).

According to the boundary conditions of the deformed wall FG, i.e.,

$$\begin{aligned} &x = 0 \text{ at } \ y = 0, \\ &\tfrac{dx}{dy} = 0 \text{ at } y = \tfrac{h_0}{2}, \\ &M = S\tfrac{dx}{dy} \ \text{ at } \ y = 0. \end{aligned} \tag{33}$$

These boundary conditions giving the following equations for determining the constants A and B in Eq. (32):

$$\begin{cases} B + \frac{M}{P} = 0 \\ A\lambda\cos\frac{(\lambda h_0)}{2} - B\lambda\sin\frac{(\lambda h_0)}{2} = 0 \\ M = SA\lambda. \end{cases} \tag{34}$$

Investigating the possibility of curved forms of equilibrium, we observe that the only way to have a nontrivial solution of the three equations in Eq. (34) is to have determinant of the coefficients equal to zero. This determinant is

$$\begin{vmatrix} 0 & 1 & \frac{1}{P} \\ \lambda\cos\frac{(\lambda h_0)}{2} & -\lambda\sin\frac{(\lambda h_0)}{2} & 0 \\ S\lambda & 0 & -1 \end{vmatrix}, \tag{35}$$

and setting it equal to zero gives

$$\tan\frac{(\lambda h_0)}{2} = -(\lambda h_0)\frac{E_0 I_0'}{S h_0}. \tag{36}$$

Substituting Eq. (31) into Eq. (36), we find

$$\tan\frac{(\lambda h_0)}{2} = -(\lambda h_0)\frac{l_0}{4h_0}. \tag{37}$$

To solve Eq. (37), a graphical method is useful. The smallest root $(\lambda h_0)_{min}$ of Eq. (37) can be obtained. Thus, the according critical load of the vertical wall FG is

$$P_{crit}^{FG} = \frac{[(\lambda h_0)_{min}]^2 E_0 I_0'}{h_0^2}, \tag{38}$$

According to the results of Timoshenko and Gere [31], the critical load of the wall FG, i.e., Eq. (38), can be expressed as

$$P_{crit}^{FG} = \frac{n_0^2 \pi^2 E_0 I_0'}{h_0^2}, \tag{39}$$

where $n_0 = \frac{(\lambda h_0)_{min}}{\pi}$ is defined as the end constraint factor that depends on the degree of constraint to rotation at the end nodes F and G, and $0.5 \leqslant n_0 \leqslant 2$, in which $n_0 = 0.5$ if rotation is freely allowed, e.g., pinned joints, and $n_0 = 2$ if rotation is inhibited as in the case of fixed ends. It can be seen from Eqs. (37)–(39) that, values of n_0 only dependent on h_0/l_0.

For the reinforcing walls, a similar solution form as Eq. (39) can be expressed for their critical load,

$$P_{crit}^{r} = \frac{n_1^2 \pi^2 E_1 I_1}{l_1^2}, \tag{40}$$

With $I_1 = bt_1^3/12$ is the second moment of inertia of the cross section of the reinforcing walls.

Since the ends of the reinforcing walls are restrained by the vertical and the slant walls greatly, as shown in Fig. 10b, hence, $n_1 = 2$ is used here to estimate the critical load of them, i.e.,

$$P_{crit}^{r} = \frac{4\pi^2 E_1 I_1}{l_1^2}. \tag{41}$$

Thus, the critical load of the representative unit as shown in Fig. 11a is

$$P_{crit} = P_{crit}^{FG} + 2P_{crit}^{r}\sin\theta_1 \tag{42}$$

So that, the critical nominal stress of the new proposed honeycomb is

$$\sigma_{crit} = \frac{P_{crit}}{2l_0\cos\theta_0}. \tag{43}$$

Fig. 12 shows a comparison of critical buckling stress of both the new honeycomb and NRHH between the analytical predictions and the numerical simulations. The plateau of the compressive stress-strain curves obtained from numerical simulations in Fig. 12 is caused by the elastic buckling. It is remarkable that, the critical buckling strength of the NRHH is lower than that of the new honeycomb under different re-entrant angle θ_0, and for both the new honeycomb and the NRHH, the re-entrant angle θ_0 have significant effect on the critical buckling strength. For increasing the re-entrant angle θ_0, the critical buckling strength increase. Obviously, the present analytical predictions are close to the numerical results, which verifying the theoretical framework. Of course, there are errors between the present analytical predictions and numerical simulations. This can be explained by the following reasons. The change in θ_0 during the honeycomb's deformation and the rotation constraint of the reinforcing walls on the vertical wall's end-points are neglected. The fixed ends assumption on the reinforcing walls, i.e., $n_1 = 2$ in Eq. (40), may lead to an overestimation on the critical strength of the new honeycomb. In addition, in the present theoretical framework, the relative displacement in horizontal direction between the two end points F and G is assumed to be zero under any value of the re-entrant angle θ_0. Actually, the relative displacement is related to θ_0. The smaller the re-entrant angle θ_0 is, the smaller the relative horizontal displacement as the horizontal constraint of the reinforcing walls on the end points of wall FG increase with the decrease of θ_0.

In our design, the reinforcing walls play a significant role to the buckling strength improving. On the one hand, the reinforcing walls could bear a part of the vertical load directly; on the other hand, the restraint of the reinforcing walls on the end points of vertical walls can improve the critical load of them. The degree of constraint on the end nodes of vertical walls caused by the reinforcing walls is measured by end constraint factor. In Gibson and Ashby's work [1], several end constraint factors for elastic bucking of honeycomb with hexagonal cells were derived. Similar analysis is easily performed for the normal re-entrant hexagonal honeycomb (NRHH). Here, the NRHH and the new honeycomb with the same values of h_0/l_0 are investigated. The dependence of constraint factors for elastic bucking of these two configurations on h_0/l_0 are displayed in Fig. 13. As it can be seen from Fig. 13 that, $n_0 \geqslant 2n^*$ under various value of h_0/l_0, which reveals that the critical buckling load of the vertical walls of the new honeycomb is much higher than that of the NRHH.

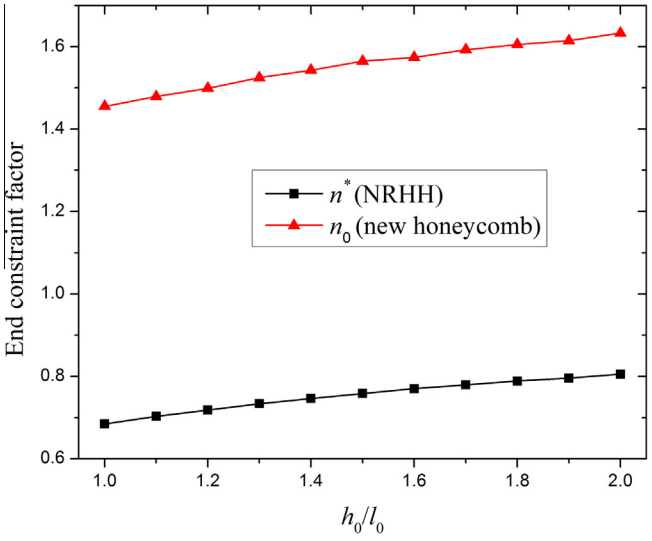

Fig. 13. Variation of the end constraint factors with h_0/l_0.

5. Conclusion

Auxetic materials present a series of particular characteristics in comparison to conventional materials, such as enhancement of shear modulus, indentation resistance, and fracture toughness. However, the in-plane stiffness of them is relatively low. In this

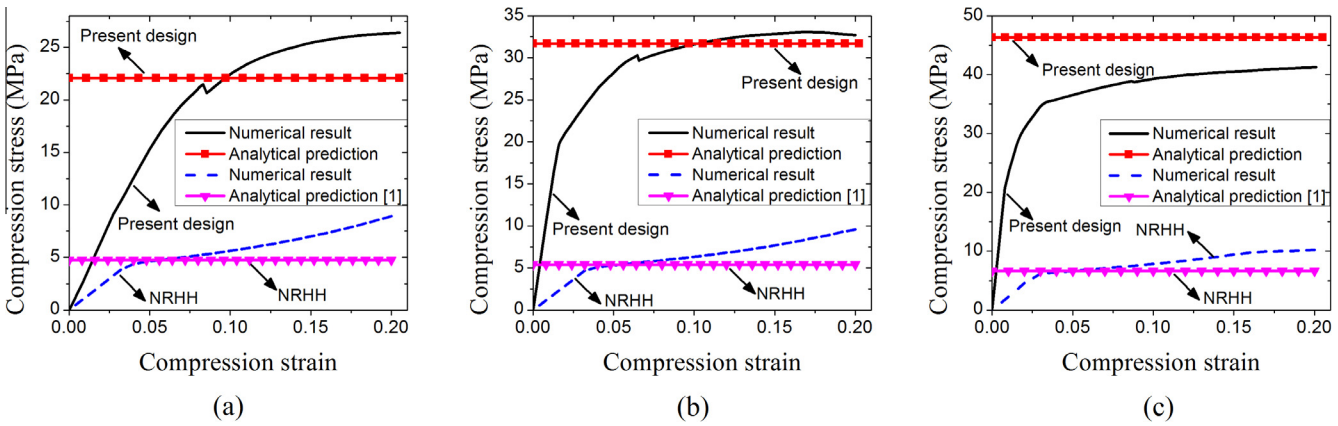

Fig. 12. Comparisons of critical buckling strength between analytical and numerical results ($t_0 = 1, t_1 = 0.5, l_0 = 10, h_0 = 20$) (a) $\theta_0 = 10^\circ$, (b) $\theta_0 = 30^\circ$ and (c) $\theta_0 = 45^\circ$.

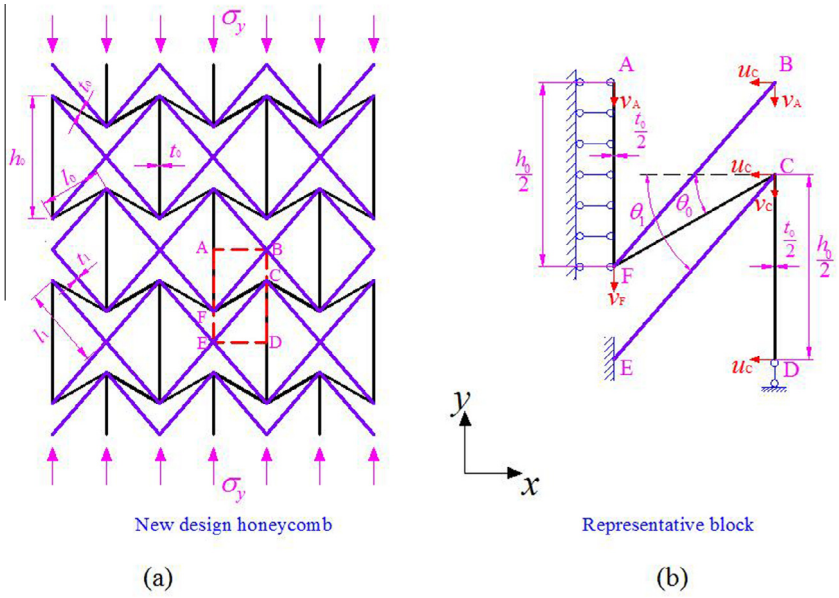

Fig. 14. (a) New honeycomb under uniaxial compression along the *y*-direction and (b) representative block.

paper, a novel honeycomb, comprised of re-entrant hexagonal configuration and rhombic configuration, is developed. The new structure can be regarded as an optimization to the NRHH by embedding four reinforcing walls into every cell of it. The in-plane effective modulus, i.e., the Young's modulus and Poisson's ratio, of the new honeycomb are analytically derived, which later verified by finite element simulations. Both the results obtained from the analytical and numerical analysis reveal that the new honeycomb can achieve negative Poisson's ratio and the in-plane effective Young's modulus of it is significantly improved compared to the NRHH.

The dependence of the in-plane elastic constants on the re-entrant angle θ_0, the cell wall length ratio h_0/l_0, normalized axial rigidity of the reinforcing walls $(E_1A_1)/(E_0A_0)$ and the relative density ρ^*/ρ_0 are further studied by using the numerically validated analytical solutions. With respect to the NRHH, the new proposed structure allows more geometric parameters in the unit cell, which provide enhanced in-plane flexibility and tailoring of properties. Results show that, for maintaining a superior auxetic performance, the reinforcing walls should be designed with appropriate axial rigidity. A comparison of in-plane stiffness is carried out between the present design and other periodic topologies. The results reveal that the new honeycomb developed in this paper shows superior stiffness and auxetic behavior with respect to the others.

Critical buckling strength of the new honeycomb under uniaxial compression is investigated analytically and numerically. The results obtained from the analytical analysis are close to that obtained from numerical simulations. Both of them reveal that the critical buckling strength of the new structure is much higher than that of the NRHH.

For these outstanding properties mentioned above, this layout may provide a new concept for the optimization and design of auxetic materials.

Acknowledgments

This work was supported by the National Natural Science Foundation of China (Grant Numbers 11472314, 11172335 and 11172334), the opening project of State Key Laboratory of Explosion Science and Technology (Beijing Institute of Technology) (Grant Number KFJJ14-4M).

Appendix A. In-plane elastic properties in direction *y*

As shown in Fig. 14, when the new honeycomb is uniaxially compressed by a stress σ_y along the *y*-direction, uniform vertical displacement v_A will be caused at points A and B, a uniform horizontal displacement u_C will be caused at point B and wall CD, while a vertical displacement v_C at point C and v_F at point F, respectively. Similar to the analyses performed for compressing along the *x*-direction, the axial force on walls CD and FA is

$$F^N_{CD} = F^N_{FA} = \frac{E_0 b t_0}{h_0} v_C. \tag{A-1}$$

The axial force on walls EC and FB is

$$F^N_{EC} = F^N_{FB} = \frac{E_1 b t_1}{l_1}(u_C \cos\theta_1 + v_C \sin\theta_1). \tag{A-2}$$

The axial force on FC is

$$F^N_{FC} = \frac{E_0 b t_0}{l_0}[u_C \cos\theta_0 + (v_C - v_F)\sin\theta_0]. \tag{A-3}$$

The transverse shear force on FC can be obtained,

$$F^S_{FC} = \frac{E_0 b (t_0/l_0)^3 [u_C \sin\theta_0 - (v_C - v_F)\cos\theta_0]}{1 + 2.4(1+\mu_0)(t_0/l_0)^2}. \tag{A-4}$$

Along direction *x*, the structure is assumed to deform freely, the total force must be zero, i.e.

$$F^N_{FC}\cos\theta_0 + F^S_{FC}\sin\theta_0 + 2F^N_{EC}\cos\theta_1 = 0. \tag{A-5}$$

The resultant force applied at point C along direction *y* should be zero, so that,

$$F^S_{FC}\cos\theta_0 - F^N_{FC}\sin\theta_0 - F^N_{EC}\sin\theta_1 - F^N_{CD} = 0. \tag{A-6}$$

According to Eqs. (A-5) and (A-6), we have,

$$v_C = \frac{K'_1 + K'_2}{K'_3 + K'_4} u_C, \tag{A-7}$$

with

$$K_1' = \frac{E_0 t_0}{l_0}\left[\frac{(t_0/l_0)^2\cos^2\theta_0}{1+2.4(1+\mu_0)(t_0/l_0)^2}+\sin^2\theta_0\right] \times\left[\frac{\cos^2\theta_0 E_0 t_0}{l_0}+\frac{E_0(t_0/l_0)^3\sin^2\theta_0}{1+2.4(1+\mu_0)(t_0/l_0)^2}+\frac{2\cos^2\theta_1 E_1 t_1}{l_1}\right],$$

$$K_2' = \frac{\sin\theta_0\cos\theta_0 E_0 t_0\left[1+(1.4+2.4\mu_0)(t_0/l_0)^2\right]}{l_0\left[1+2.4(1+\mu_0)(t_0/l_0)^2\right]} \times\left[\frac{\sin\theta_0\cos\theta_0 E_0 t_0\left[-1-(1.4+2.4\mu_0)(t_0/l_0)^2\right]}{l_0\left[1+2.4(1+\mu_0)(t_0/l_0)^2\right]}-\frac{\sin\theta_1\cos\theta_1 E_1 t_1}{l_1}\right],$$

$$K_3' = \left(\frac{\sin^2\theta_1 E_1 t_1}{l_1}+\frac{E_0 t_0}{h_0}\right) \times\frac{E_0 t_0\sin\theta_0\cos\theta_0\left[1+(1.4+2.4\mu_0)(t_0/l_0)^2\right]}{l_0\left[1+2.4(1+\mu_0)(t_0/l_0)^2\right]},$$

$$K_4' = \frac{-2\sin\theta_1\cos\theta_1 E_1 t_1}{l_1}\left[\frac{E_0(t_0/l_0)^3\cos^2\theta_0}{1+2.4(1+\mu_0)(t_0/l_0)^2}+\frac{\sin^2\theta_0 E_0 t_0}{l_0}\right].$$

The vertical displacement at point F is

$$v_F = \frac{\cos^2\theta_0 E_0 t_0/l_0 + E_0(t_0/l_0)^3\sin^2\theta_0/[1+2.4(1+\mu_0)(t_0/l_0)^2]+2\cos^2\theta E_1 t_1/l_1}{\{E_0 t_0/l_0 - E_0(t_0/l_0)^3/[1+2.4(1+\mu_0)(t_0/l_0)^2]\}\sin\theta_0\cos\theta_0}u_C + \frac{\sin\theta_0\cos\theta_0 E_0 t_0/l_0 - \sin\theta_0\cos\theta_0 E_0(t_0/l_0)^3/[1+2.4(1+\mu_0)(t_0/l_0)^2]}{\{E_0 t_0/l_0 - E_0(t_0/l_0)^3/[1+2.4(1+\mu_0)(t_0/l_0)^2]\}\sin\theta_0\cos\theta_0}\frac{K_1'+K_2'}{K_3'+K_4'}u_C + \frac{2\sin\theta_1\cos\theta_1 E_1 t_1/l_1}{\{E_0 t_0/l_0 - E_0(t_0/l_0)^3/[1+2.4(1+\mu_0)(t_0/l_0)^2]\}\sin\theta_0\cos\theta_0}\frac{K_1'+K_2'}{K_3'+K_4'}u_C, \tag{A-8}$$

Since the resultant force applied at points A and B along direction y should be zero, then we have

$$\frac{E_0 b t_0(K_1'+K_2')}{h_0(K_3'+K_4')}u_C+\frac{E_1 b t_1}{l_1}\left[\sin\theta_1\cos\theta_1+\frac{(K_1'+K_2')\sin^2\theta_1}{(K_3'+K_4')}\right]u_C = \sigma_y l_0\cos\theta_0 b, \tag{A-9}$$

So that,

$$\sigma_y = \frac{E_0 t_0(K_1'+K_2')}{h_0 l_0\cos\theta_0(K_3'+K_4')}u_C + \frac{E_1 t_1}{l_1 l_0\cos\theta_0}\left[\sin\theta_1\cos\theta_1+\frac{(K_1'+K_2')\sin^2\theta_1}{(K_3'+K_4')}\right]u_C, \tag{A-10}$$

The strain along the y-direction is

$$\varepsilon_y = \frac{E_0\cos^2\theta_0 t_0/l_0 + E_0(t_0/l_0)^3\sin^2\theta_0/[1+2.4(1+\mu_0)(t_0/l_0)^2]+2\cos^2\theta_1 E_1 t_1/l_1}{\{E_0 t_0/l_0 - E_0(t_0/l_0)^3/[1+2.4(1+\mu_0)(t_0/l_0)^2]\}l_0\sin\theta_0\cos\theta_0(h_0/l_0-\sin\theta_0)}u_C + \frac{2\sin\theta_0\cos\theta_0\{E_0 t_0/l_0 - E_0(t_0/l_0)^3/[1+2.4(1+\mu_0)(t_0/l_0)^2]\}\frac{K_1'+K_2'}{K_3'+K_4'}}{\{E_0 t_0/l_0 - E_0(t_0/l_0)^3/[1+2.4(1+\mu_0)(t_0/l_0)^2]\}l_0\sin\theta_0\cos\theta_0(h_0/l_0-\sin\theta_0)}u_C + \frac{(2\sin\theta_1\cos\theta_1 E_1 t_1/l_1)\frac{K_1'+K_2'}{K_3'+K_4'}}{\{E_0 t_0/l_0 - E_0(t_0/l_0)^3/[1+2.4(1+\mu_0)(t_0/l_0)^2]\}l_0\sin\theta_0\cos\theta_0(h_0/l_0-\sin\theta_0)}u_C \tag{A-11}$$

The strain along x-direction is

$$\varepsilon_x = \frac{u_C}{l_0\cos\theta_0}. \tag{A-12}$$

The effective Young's modulus and Poisson's ratio along the y-direction is

$$E_y = \frac{\sigma_y}{\varepsilon_y}, \tag{A-13}$$

and

$$\mu_{yx} = -\frac{\varepsilon_x}{\varepsilon_y}. \tag{A-14}$$

The ratio of β_y is

$$\beta_y = \frac{E_y}{E_y^*}. \tag{A-15}$$

References

[1] Gibson LJ, Ashby MF. Cellular solids: structure and properties. London: Pergamon Press; 1988.
[2] Wang AJ, Mcdowell DL. In-plane stiffness and yield strength of periodic metal honeycombs. J Eng Mater Technol 2004;126(2):137–56.
[3] Niu B, Wang B. Directional mechanical properties and wave propagation directionality of Kagome honeycomb structures. Eur J Mech A Solids 2016;57:45–58.
[4] Hu LL, Yu TX. Mechanical behavior of hexagonal honeycombs under low-velocity impact – theory and simulations. Int J Solids Struct 2013;50(20–21):3152–65.
[5] Hu LL, You FF, Yu TX. Effect of cell-wall angle on the in-plane crushing behaviour of hexagonal honeycombs. Mater Des 2013;46(4):511–23.
[6] Hu LL, You FF, Yu TX. Analyses on the dynamic strength of honeycombs under the y -directional crushing. Mater Des 2014;53(1):293–301.
[7] Masters IG, Evans KE. Models for the elastic deformation of honeycombs. Compos Struct 1996;35(4):403–22.
[8] Grima JN, Attard D, Ellul B, Gatt R. An improved analytical model for the elastic constants of auxetic and conventional hexagonal honeycombs. Cell Polym 2011;30(6):287–310.
[9] Scarpa F, Panayiotou P, Tomlinson G. Numerical and experimental uniaxial loading on in-plane auxetic honeycombs. J Strain Anal Eng Des 2000;35(5):383–8.
[10] Hu LL, Deng H. Indentation resistance of the re-entrant hexagonal honeycombs with negative poisson's ratio. Mater Res Innovations 2015;19(S1). S1-442–S1-445.
[11] Wan H, Ohtaki H, Kotosaka S, Hu GM. A study of negative Poisson's ratios in auxetic honeycombs based on a large deflection model. Eur J Mech A Solids 2004;23(1):95–106.
[12] Fu MH, Xu OT, Hu LL, Yu TX. Nonlinear shear modulus of re-entrant hexagonal honeycombs under large deformation. Int J Solids Struct 2015;80:284–96.
[13] Bezazi A, Scarpa F, Remillat C. A novel centresymmetric honeycomb composite structure. Compos Struct 2005;71:356–64.
[14] Bückmann T, Stenger N, Kadic M, Kaschke J, Frölich A, Kennerknecht T, Eberl C, Thiel M, Wegener M. Tailored 3D mechanical metamaterials made by dip-in direct-laser-writing optical lithography. Adv Mater 2012;24:2710–4.
[15] Yang L, Cormier D, West H, Harrysson O, Knowlson K. Non-stochastic Ti–6Al–4V foam structures with negative Poisson's ratio. Mater Sci Eng, A 2012;558:579–85.
[16] Yang L, Harrysson O, West H, Cormier D. Modeling of uniaxial compression in a 3D periodic re-entrant lattice structure. J Mater Sci 2013;48(4):1413–22.
[17] Yang L, Harrysson O, Cormier D, West H, Gong H, Stucker B. Additive manufacturing of metal cellular structures: design and fabrication. Jom J Miner Met Mater Soc 2015;67(3):608–15.
[18] Yang L, Harrysson O, West H, Cormier D. Mechanical properties of 3D re-entrant honeycomb auxetic structures realized via additive manufacturing. Int J Solids Struct 2015;69–70:475–90.
[19] Chuang CH, Huang JS. Effects of solid distribution on the elastic buckling of honeycombs. Int J Mech Sci 2002;44(44):1429–43.
[20] Haghpanah Babak, Papadopoulos Jim, Mousanezhad Davood, Nayeb-Hashemi Hamid, Vaziri Ashkan. Buckling of regular, chiral and hierarchical honeycombs under a general macroscopic stress state. Proc R Soc A Math Phys Eng Sci 2014;470(2167):20130856.
[21] Carneiro VH, Meireles J, Puga H. Auxetic materials — a review. Mater Sci Poland 2013;31(4):561–71.
[22] Prawoto Y. Seeing auxetic materials from the mechanics point of view: a structural review on the negative Poisson's ratio. Comput Mater Sci 2012;58:140–53.
[23] Jones D. Handbook of viscoelastic vibration damping. New York: John Wiley and Sons; 2001.
[24] Assidi M, Ganghoffer JF. Composites with auxetic inclusions showing both an auxetic behavior and enhancement of their mechanical properties. Compos Struct 2012;94:2373–82.
[25] Lira C, Scarpa F. Transverse shear stiffness of thickness gradient honeycombs. Compos Sci Technol 2010;70(6):930–6.
[26] Hou Y, Neville R, Scarpa F, Remillat C, Gu B, Ruzzene M. Graded conventional-auxetic Kirigami sandwich structures: flatwise compression and edgewise loading. Compos B Eng 2014;59(3):33–42.

[27] Boldrin L, Hummel S, Scarpa F, Di Maio D, Lira C, Ruzzene M, Remillat CDL, Lim TC, Rajasekaran R, Patsias S. Dynamic behaviour of auxetic gradient composite hexagonal honeycombs. Compos Struct 2016;149:114–24.
[28] Zied K, Osman M, Elmahdy T. Enhancement of the in-plane stiffness of the hexagonal re-entrant auxetic honeycomb cores. Phys Status Solidi B 2015;252 (12):2685–92.
[29] Lu ZX, Li X, Yang ZY, Xie F. Novel structure with negative Poisson's ratio and enhanced Young's modulus. Compos Struct 2016;138:243–52.
[30] Grenestedt JL. Effective elastic behavior of some models for perfect cellular solids. Int J Solids Struct 1999;36(10):1471–501.
[31] Timoshenko SP, Gere JM. Theory of elastic stability. 2nd ed. New York: McGraw-Hill; 1961.